EES Solar



COMMUNICATION

View Article Online
View Journal



Cite this: DOI: 10.1039/d5el00105f

Received 30th June 2025 Accepted 23rd August 2025

DOI: 10.1039/d5el00105f

rsc.li/EESSolar



Julien Hurni, (1) †** Kerem Artuk, (1) †** Thibault Schaller, a Jonathan S. Austin, Reyu Sakakibara, Bertrand Paviet-Salomon, Audrey Morisset, Fan Fu, (1) Christophe Ballif, (1) ab Christian M. Wolff (1) and Franz-Josef Haug (1) a

We demonstrate high-efficiency perovskite–silicon tandem solar cells using double-sided tunnel oxide passivated contacts (TOPCon²) bottom cells, achieving 30.2% efficiency on both-sides flat and 31.3% on front-textured devices. The former is enabled by high passivation quality on flat surfaces and the latter by enhanced optical performance. These results highlight that TOPCon² is a promising platform for scalable tandem integration beyond silicon heterojunction-based bottom cells.

Introduction

Crystalline silicon (c-Si) solar cells account for approximately 98% of the global photovoltaics (PV) market, driven by their high efficiency, long-term stability, and low production costs.¹ Although back-contacted silicon heterojunction (SHJ) cells have reached record efficiencies of 27.8%,² tunnel oxide passivated contact (TOPCon) technology is gaining industry preference due to its low cost of ownership. As a result, TOPCon is expected to reach over 70% of global production by 2026.

As single-junction c-Si cells approach their 29.6% efficiency limit, ³ further improvements depend on tandem architectures. These combine absorbers with complementary band gaps to minimize thermalization losses and improve spectral utilization. ⁴ Among these, perovskite–Si tandems have emerged as the most promising option, with efficiencies approaching 35%. Although top-performing tandems currently use SHJ bottom cells, commercial interest is shifting toward TOPCon-based tandems. Notably, Jinko Solar achieved 33.8% (1 cm²) and QCells 28.6% (M10, 330 cm²) efficiencies. Double-sided TOPCon (TOPCon²) cells⁵⁻⁹—with poly-Si contacts on both front and

Broader context

As conventional crystalline silicon (c-Si) solar cells approach their efficiency limits, perovskite–silicon tandem solar cells have emerged as the next frontier in photovoltaics, pushing efficiencies beyond 30%. This work significantly advances the field by demonstrating highly efficient perovskite–TOPCon 2 silicon tandem devices, achieving a remarkable 31.3% efficiency on front-textured cells. The key breakthrough lies in optimizing TOPCon 2 cells as the bottom cell platform, which offers compatibility with existing manufacturing lines. Crucially, the research uses an AlO_x-based hydrogenation method. This method overcomes the limitations of conventional processes by preventing damage to the sensitive tunnel oxide layer during fabrication, particularly for textured surfaces. This allows for superior passivation quality and improved light trapping, paving the way for more efficient and cost-effective solar energy conversion.

rear—offer a promising bottom-cell platform for perovskite–Si tandem integration. These simplify junction formation, enhance passivation, and are compatible with existing production lines.

In this contribution, we show the optimization of TOPCon² bottom cells integrated into high-efficiency perovskite–Si tandem devices with 30% efficiency on silicon wafers flat on both sides, and over 31% on front-textured rear-flat devices. The result of 30.2% is enabled by the high passivation of the poly-Si(n) and poly-Si(p) layers on flat surfaces. The superior performance of the textured devices is attributed not only to improved optical response from front texturing, but also to the high passivation quality of the poly-Si(n) contact enabled by AlO_x-based hydrogenation.

Results

Conventionally, our hydrogenation process involves the deposition of a \sim 70 nm thick silicon nitride (SiN $_x$) layer, followed by a rapid thermal annealing step at approximately 800 °C. This process enables releasing hydrogen that subsequently diffuses into the silicon bulk. However, the SiN $_x$ layer must be removed before the deposition of the interconnection layer—typically via

^aEcole Polytechnique Fédérale de Lausanne, Institute of Electrical and Micro Engineering, Photovoltaics and Thin Films Electronics Laboratory (PV-Lab), Neuchâtel, Switzerland. E-mail: julien.hurni@epfl.ch

 $[^]b$ Centre Suisse d'Electronique et Microtechnique (CSEM), Sustainable Energy Center, Neuchâtel, Switzerland

^{&#}x27;Swiss Federal Laboratories for Materials Science and Technology (EMPA), Laboratory for Thin Films and Photovoltaics, Switzerland

[†] These authors contributed equally.

EES Solar

immersion in hydrofluoric acid (HF) for 30 minutes. The description of the processing method and sample structure can be found in the SI (Fig. S15). This prolonged HF exposure risks damaging the tunnel oxide in poly-Si contacts especially on textured surfaces. To avoid passivation damage, we introduce an alternative hydrogenation method based on the deposition of a thin (10 nm) aluminum oxide (AlO_x) layer via atomic layer deposition (ALD) followed by an annealing at \sim 400 °C. ¹⁰ The influence of the AlO_x thickness is displayed in Fig. S2. ALD-AlO_x is removed by a rapid (\sim 30 s) HF dip because the AlO_x layer is thinner and has a significantly higher etch rate than SiN_r (Fig. S5). We evaluate the effectiveness of this method in comparison to the standard SiNx-based hydrogenation and to a no-hydrogenation control, using both fully planar and frontside nanotextured¹¹ TOPCon² structures (Fig. S1, S2, S3, S6 and S9). Our findings show that for flat devices, incorporating a hydrogenation step yields only a modest efficiency improvement ($\sim 0.2\%$ absolute in single junction Fig. S9), offering limited justification given the added complexity. In contrast, for nanotextured devices, the standard hydrogenation process leads to significant degradation in performance, likely due to damage to the tunnel SiO_r layer caused by extended HF exposure (Fig. S3). In this case, the AlO_x-based method proves to be superior, enabling implied open-circuit voltages (iVoc) as high as 740 mV—substantially higher than the ~700 mV obtained from untreated control samples (Fig. S1). The ToF-SIMS depth profile (Fig. S4) shows a hydrogen accumulation at the SiO_x/c-Si interface after AlO_r hydrogenation treatment similar to what

We then fabricate 1 cm² perovskite–Si tandem cells using flat and nanotextured TOPCon² bottom cells, as shown in the SEM images (Fig. 1(a) and (b)). The top cell structure follows our previous designs, $^{16-19}$ with a 20 nm sputtered ITO layer used for interconnection. Since poly-Si contacts are susceptible to plasma damage during sputtering, 20 a post-sputtering thermal curing step at 300 °C is introduced to recover passivation quality (Fig. S5). With this treatment and optimized hydrogenation, we achieve bottom cell $iV_{\rm oc}$ values (at 1 sun) of 726 mV (flat) and 722 mV (textured), using front-side ITO recombination layers and rear ITO/Ag contacts.

has been reported for SiNx-based hydrogenation. This allows to

reduce surface recombination (lower J_{0s} , Fig. S2 and S3), espe-

cially on nanotextured surfaces, and increase iV_{oc} . ¹²⁻¹⁵

To ensure effective current matching with the underlying silicon sub-cells, two distinct perovskite absorber bandgaps and thicknesses are employed. For flat-bottom cells, a high-bandgap ($\sim\!1.67$ eV) perovskite (Cs_0.05(FA_0.9 MA_0.1)_0.95Pb(I_0.75Br_0.25)_3 + 3% (MAPbCl_3)) ($\sim\!500$ nm) is used to leverage the high open-circuit voltage potential. In contrast, on nanotextured substrates, a relatively thicker ($\sim\!700$ nm) perovskite absorber with a lower bandgap of $\sim\!1.64$ eV (Cs_0.05(FA_0.9MA_0.1)_0.95Pb(I_0.80Br_0.20)_3 + 3% (MAPbCl_3)) is applied to enhance light absorption and optimize photocurrent distribution between the sub-cells. Fig. 1(c) presents the current–voltage characteristics and maximum power point (MPP) tracking data of the best-performing (champion) devices, along with the median performance across each fabrication batch. The performance difference between reverse and forward scan curves at the scan rates utilized in this work

(approximately 100 mV s⁻¹) is negligible. The efficiency of the tandems over several batches is displayed in Fig. S11 and S12. External quantum efficiency (EQE) spectra are shown in Fig. 1(d). While initial developments were carried out on flat samples, upon switching to nanotextured samples we simultaneously reduce the C_{60} thickness, which lowers parasitic absorption and improves the response.

Using a fully flat, hydrogenation-free TOPCon² bottom cell, we achieve 30.2% tandem efficiency-enabled by excellent passivation (i $V_{oc} = 0.71 \text{ V}$) at half-sun for the bottom cell, and top-cell i $V_{\rm oc}$ ~1.29 V, with loss-free transfer into devices achieving an average tandem $V_{\rm oc} > 2.0$ V. This demonstrates that high-efficiency perovskite-Si tandems can be fabricated using simplified processes (Fig. S15). However, current density is limited to 18.6 mA cm⁻² due to the high reflection losses induced by the flat bottom cell. For front nanotextured bottom cells, with AlO_x-based hydrogenation, we report a champion efficiency of 31.3%. Front texturing significantly improves light trapping, yielding a 1.5 mA cm⁻² current gain in the bottom cell (when integrated from 775-1200 nm, as some current is lost to the top cell). Fig. S12 shows the comparison of the different hydrogenation methods tested (i.e., no hydrogenation, SiN_x/ firing, AlOx/hotplate) when applied in tandem devices (different batches). SiN_x/firing hydrogenation leads to poor efficiencies due to the damage to the bottom cells formed during the removal of the SiN_r. The control samples (without hydrogenation) perform well reaching efficiencies up to 29%. Finally adding AlO_r/hotplate hydrogenation, allows for increasing the $V_{\rm oc}$ leading to the 31% efficiency reported.

We then evaluated the stability of the perovskite–TOPCon tandem devices. First, both front-nanotextured and fully flat tandems exhibited relatively good shelf stability when stored in the dark under N₂ atmosphere (Fig. S13). However, the front-textured devices showed slightly inferior shelf stability compared to the fully flat devices, consistent with the observations reported by Turkay *et al.*²¹

Next, we investigated the operational stability of an unencapsulated front-textured tandem cell 4 months after fabrication (while during this time the cell was stored in the dark in a N₂ environment) by simulating day-night cycling. The unencapsulated device (see Fig. S14(g) for the optical image of the cell) was stressed under maximum power point tracking (MPPT) at 1-sun illumination, 25 °C, and approximately 40% relative humidity (RH). The cell initially showed a reverse-scan efficiency of 28.9%, and after ~12 hours of continuous MPPT operation, the efficiency only decreased slightly to 28.5% (see Fig. S14). After being stored in the dark for 10 hours, the cell exhibited an efficiency of 28%, indicating no significant dark recovery, which contrasts with our previous findings.16 Interestingly, following the dark J-V and pseudo-J-V measurements before the second light cycling, the device degraded abruptly to 23.5% efficiency. During these measurements, where the voltage sweep extended up to 2.0 V, the forward-bias injection current reached 25 mA cm⁻². We hypothesize that this degradation is facilitated by carrier injection, as similar accelerated degradation under dark forward bias has been reported by Erdil et al.22 In a subsequent MPPT cycle lasting 17 hours, the device Communication EES Solar

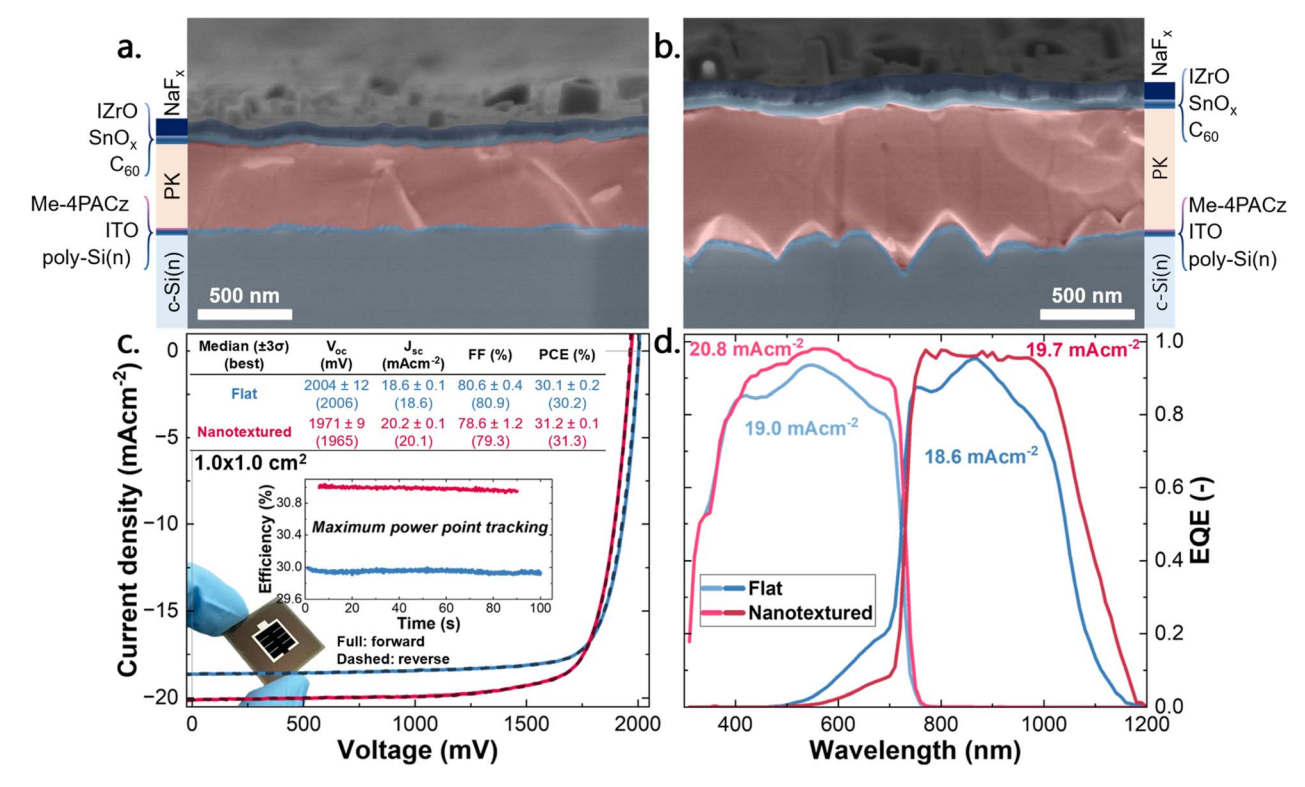


Fig. 1 (a and b) SEM cross-section of the top/bottom cell interface showing the perovskite absorber on flat and nanotextured bottom cells with the colors and the schematics indicating the layers. (c) J-V-curves of the champion devices (dashed lines forward, full lines reverse scan) on fully flat and front nanotextured bottom cell with MPP tracking measurement. The table displays the main J-V parameters (V_{oc} , J_{sc} , FF and PCE) from the two batches including the best-performing cells in brackets. (d) EQE spectra of the tandem devices on fully flat and front nanotextured bottom cells

experienced an additional $2.2\%_{abs}$ efficiency loss. Although dark measurements before the third cycle again caused further degradation, the impact was less severe than before. After a third round of light cycling, the efficiency dropped significantly to 13.6%.

Optical image (see Fig. S14(g)) and visual inspection revealed no visible signs of degradation, such as PbI_2 -related decomposition by-products, despite the unencapsulated testing in ambient air. These results underscore the importance of developing tandem solar cells that are not only stable under standard operating conditions but also resilient to a wide range of electrical stresses, including forward bias conditions commonly encountered during electroluminescence (EL) imaging of PV modules.

These 1 cm² lab-scale devices are limited by low bottom cell shunt resistance and a high local ideality factor. We attribute both to edge-related losses: the full-area passivating contacts ($\sim\!1000~\Omega~\text{sq}^{-1}$) are more conductive than the nanocrystalline silicon (nc-Si) or amorphous silicon (a-Si) layers used in SHJ bottom cells, thereby electrically coupling the active region to the inactive area and to unpassivated edges (Fig. S10). Further gains are expected from patterning the passivating contacts to the active cell area while applying insulating passivation layers to the inactive regions or when scaling up the active area. This will be part of the next steps as well as evaluating the long-term stability of the tandem devices. In parallel, we will focus on

replacing the ITO recombination layer with a p-doped silicon layer to enable indium-free bottom cells.

Conclusions

These results demonstrate that $TOPCon^2$ bottom cells enable the fabrication of high-efficiency perovskite–Si tandem devices using industrially relevant process flows. The use of AlO_x hydrogenation preserves surface passivation on textured surfaces which in turn increases optical response. With demonstrated efficiencies exceeding 31%, $TOPCon^2$ is a strong candidate for next-generation Pk-Si tandems.

Author contributions

The manuscript was written through contributions of all authors. All authors have given approval to the final version of the manuscript. Conceptualization, J. H., K. A., A. M., B. PS., C. M. W., and FJ. H; methodology, J. H., and K. A; validation, J. H., and K. A; investigation, J. H., K. A., T. S., J. S. A and R. S; writing – original draft, J. H. and K. A; writing – review & editing, J. H., K. A., T. S., J. S. A, R. S., B. PS., A. M., F. F., C. B., C. M. W. and FJ. H; visualization, J. H.; supervision, B. PS., A. M., F. F., C. B., C. M. W. and FJ. H; funding acquisition, B. PS., A. M., F. F., C. B., C. M. W. and FJ. H; funding acquisition, B. PS., A. M., F. F., C. B., C. M. W. and FJ. H.

Conflicts of interest

There are no conflicts to declare.

Data availability

SI material and all data can be found here: https://doi.org/10.5281/zenodo.15804278. Supplementary information: IV, EQE, MMP tracking, SEM. See DOI: https://doi.org/10.1039/d5el00105f.

Notes and references

- 1 ITRPV report, 2024, https://www.vdma.org/international-technology-roadmap-photovoltaic.
- 2 Longi Solar, https://www.longi.com/us/news/longi-world-record-efficiency-of-monocrystalline-silicon-cells/.
- 3 S. Schäfer and R. Brendel, Accurate Calculation of the Absorptance Enhances Efficiency Limit of Crystalline Silicon Solar Cells with Lambertian Light Trapping, *IEEE J. Photovoltaics*, 2018, 8(4), 1156–1158, DOI: 10.1109/JPHOTOV.2018.2824024.
- 4 L. C. Hirst and N. J. Ekins-Daukes, Fundamental losses in solar cells, *Prog. Photovoltaics*, 2010, **19**(3), 286–293, DOI: **10.1002/pip.1024**.
- 5 G. Nogay, J. Stuckelberger, P. Wyss, et al., Interplay of annealing temperature and doping in hole selective rear contacts based on silicon-rich silicon-carbide thin films, Sol. Energy Mater. Sol. Cells, 2017, 173, 18–24, DOI: 10.1016/j.solmat.2017.06.039.
- 6 G. Nogay, F. Sahli, J. Werner, et al., 25.1%-Efficient Monolithic Perovskite/Silicon Tandem Solar Cell Based on a p-type Monocrystalline Textured Silicon Wafer and High-Temperature Passivating Contacts, ACS Energy Lett., 2019, 4(4), 844–845, DOI: 10.1021/acsenergylett.9b00377.
- 7 B. Li, M. Härtel, A. Al-Ashouri, et al., Atomic-Layer-Deposition-Free Monolithic Perovskite/Silicon Tandem Solar Cell Reaching 29.91% Power Conversion on Industrial PERX/TOPCon-like Silicon Bottom Cells, ACS Energy Lett., 2024, 9(9), 4550–4556, DOI: 10.1021/acsenergylett.4c01502.
- 8 L. Duan, S. Pheng Phang, D. Yan, *et al.*, Over 29%-efficient, stable n-i-p monolithic perovskite/silicon tandem solar cells based on double-sided poly-Si/SiO² passivating contact silicon cells, *J. Mater. Chem. A*, 2024, **12**, 20006–20016, DOI: **10.1039/D4TA03396E**.
- 9 A. Damm, M. Bories, J. Benick, et al., Hydrogenation characteristics of p-type poly-Si passivating contacts on textured surface for double-sided TOPCon devices, Sol. Energy Mater. Sol. Cells, 2025, 285, 113542, DOI: 10.1016/ j.solmat.2025.113542.
- 10 A. Richter, J. Benick, M. Hermle and S. W. Glunz, Reaction kinetics during the thermal activation of the silicon surface passivation with atomic layer deposited Al₂O₃,

- Appl. Phys. Lett., 2014, **104**(6), 061606, DOI: **10.1063**/1.4865901.
- 11 Y. Hou, E. Aydin, M. De Bastiani, *et al.*, Efficient tandem solar cells with solution-processed perovskite on textured crystalline silicon, *Science*, 2020, 367(6482), 1135–1140, DOI: 10.1126/science.aaz3691.
- 12 B. W. H. van de Loo, *et al.*, On the hydrogenation of Poly-Si passivating contacts by Al₂O₃ and SiNx thin films, *Sol. Energy Mater. Sol. Cells*, 2020, **215**, 110592, DOI: **10.1016**/ **j.solmat.2020.110592**.
- 13 M. Schnabel, *et al.*, Hydrogen passivation of poly-Si/SiOx contacts for Si solar cells using Al₂O₃ studied with deuterium, *Appl. Phys. Lett.*, 2018, **112**(20), 203901, DOI: **10.1063/1.5031118**.
- 14 D. Kang, et al., Optimum Hydrogen Injection in Phosphorus-Doped Polysilicon Passivating Contacts, ACS Appl. Mater. Interfaces, 2021, 13(46), 55164–55171, DOI: 10.1021/ acsami.1c17342.
- 15 S. Pal, et al., Quantification of hydrogen in nanostructured hydrogenated passivating contacts for silicon photovoltaics combining SIMS-APT-TEM: A multiscale correlative approach, Appl. Surf. Sci., 2021, 555, 149650, DOI: 10.1016/ j.apsusc.2021.149650.
- 16 D. Turkay, K. Artuk, X. Y. Chin, *et al.*, Synergetic substrate and additive engineering for over 30%-efficient perovskite-Si tandem solar cells, *Joule*, 2024, **8**(6), 1735–1753, DOI: **10.1016/j.joule.2024.04.015**.
- 17 A. Harter, K. Artuk, F. Mathies, et al., Perovskite/Silicon Tandem Solar Cells Above 30% Conversion Efficiency on Submicron-Sized Textured Czochralski-Silicon Bottom Cells with Improved Hole-Transport Layers, ACS Appl. Mater. Interfaces, 2024, 16(45), 62817–62826, DOI: 10.1021/acsami.4c09264.
- 18 K. Artuk, A. Oranskaia, D. Turkay, *et al.*, 60 cm² perovskite-silicon tandem solar cells with an efficiency of 28.9% by homogenous passivation, *Nat. Commun.*, 2025, DOI: 10.1038/s41467-025-63673-y.
- 19 K. Artuk, D. Turkay, M. D. Mensi, et al., A Universal Perovskite/C60 Interface Modification via Atomic Layer Deposited Aluminum Oxide for Perovskite Solar Cells and Perovskite-Silicon Tandems, Adv. Mater., 2024, 36(21), 2311745, DOI: 10.1002/adma.202311745.
- 20 K. Tao, S. Jiang, R. Jia, *et al.*, The impact of indium tin oxide deposition and post annealing on the passivation property of TOPCon solar cells, *Sol. Energy*, 2018, **176**, 241–247, DOI: **10.1016/j.solener.2018.10.034**.
- 21 D. Turkay, K. Artuk, M. Othman, *et al.*, Beyond Flat: Undulated Perovskite Solar Cells on Microscale Si Pyramids by Solution Processing, *ACS Energy Lett.*, 2025, **10**(3), 1397–1403, DOI: **10.1021/acsenergylett.5c00221**.
- 22 U. Erdil, M. Khenkin, M. Remec, et al., Mimicking Outdoor Ion Migration in Perovskite Solar Cells: A Forward Bias, No-Light Accelerated Aging Approach, ACS Energy Lett., 2025, 10(3), 1529–1537, DOI: 10.1021/acsenergylett.5c00376.